AIP | Applied Physics Letters

Guide-star-based computational adaptive optics for broadband interferometric tomography

Steven G. Adie, Nathan D. Shemonski, Benedikt W. Graf, Adeel Ahmad, P. Scott Carney, and Stephen A. Boppart

Citation: Applied Physics Letters **101**, 221117 (2012); doi: 10.1063/1.4768778
View online: http://dx.doi.org/10.1063/1.4768778
View Table of Contents: http://scitation.aip.org/content/aip/journal/apl/101/22?ver=pdfcov
Published by the AIP Publishing

Guide-star-based computational adaptive optics for broadband interferometric tomography

Steven G. Adie,[1,2] Nathan D. Shemonski,[1,2] Benedikt W. Graf,[1,2] Adeel Ahmad,[1,2] P. Scott Carney,[1,2] and Stephen A. Boppart[1,2,3]
[1]*Beckman Institute for Advanced Science and Technology, University of Illinois at Urbana-Champaign, Urbana, Illinois 61801, USA*
[2]*Department of Electrical and Computer Engineering, University of Illinois at Urbana-Champaign, Urbana, Illinois 61801, USA*
[3]*Departments of Bioengineering and Internal Medicine, University of Illinois at Urbana-Champaign, Urbana, Illinois 61801, USA*

(Received 21 August 2012; accepted 8 November 2012; published online 29 November 2012)

We present a method for the numerical correction of optical aberrations based on indirect sensing of the scattered wavefront from point-like scatterers ("guide stars") within a three-dimensional broadband interferometric tomogram. This method enables the correction of high-order monochromatic and chromatic aberrations utilizing guide stars that are revealed after numerical compensation of defocus and low-order aberrations of the optical system. Guide-star-based aberration correction in a silicone phantom with sparse sub-resolution-sized scatterers demonstrates improvement of resolution and signal-to-noise ratio over a large *isotome*. Results in highly scattering muscle tissue showed improved resolution of fine structure over an extended volume. Guide-star-based computational adaptive optics expands upon the use of image metrics for numerically optimizing the aberration correction in broadband interferometric tomography, and is analogous to phase-conjugation and time-reversal methods for focusing in turbid media.
 [http://dx.doi.org/10.1063/1.4768778]

The development of adaptive optics (AO) for both astronomy and optical microscopy is motivated by the need for wavefront control. Aberrations, or deviations from ideal optical wavefronts, reduce image resolution, and are introduced by the intervening medium between the object and the image recording plane (including optical elements of the imaging system). In terrestrial astronomy, AO utilizes a deformable mirror to dynamically compensate aberrations of the turbulent atmosphere.[1] These aberrations can be measured using distant (point) sources of light, or "guide stars," that can include naturally occurring stars or artificially generated guide stars through the focusing of high-power lasers in the upper atmosphere.[1,2] In optical microscopy, AO has been utilized to compensate monochromatic sample-induced aberrations in non-interferometric imaging,[3] as well as in optical coherence tomography.[4,5] The guide star can be generated by the (scanned and focused) imaging beam[4] or a separate static beam focused into the sample.[5] Image metrics can also be utilized to optimize the aberration correction without the use of a wavefront sensor,[6] a method known as sensor-less AO.

Interferometric measurement of the complex optical field provides an alternative to hardware-based aberration correction. This allows propagation of the optical field post-data-acquisition, enabling refocusing and numerical compensation of wavefront aberrations as is done in digital holography.[7] In broadband interferometric tomography, where the recorded signal is three-dimensional (i.e., can be written as a function of two spatial dimensions (x, y) and wavenumber k), refocusing can bring given planes of the 3D tomogram into focus.[8] Interferometric synthetic aperture microscopy (ISAM), a computed imaging method utilizing Fourier domain resampling, provides highly efficient reconstruction of 3D tomograms with spatially invariant resolution.[9,10] Until recently, the reconstruction of broadband interferometric tomograms did not account for the effects of optical aberrations.

Computational AO (CAO) is a recently developed method that utilizes the amplitude and phase information recorded within a broadband interferometric tomogram to correct the effects of optical aberrations in 3D tomograms.[11] It is based on the Fourier optics result that the pupil function, the phase of which is modified by AO hardware, is related to the complex optical field at the focal plane through a transverse Fourier transform.[12] Included in this relationship is a coordinate scaling relating the physical (x, y) coordinates of the objective lens pupil to the transverse Fourier domain coordinates (Q_x, Q_y) of the point-spread function (PSF) at focus. However, with a double-pass imaging geometry the effective PSF is the square of the illumination beam, and the corresponding effective pupil function is the convolution of the pupil functions associated with the beam. Aberrations in CAO are compensated by modifying the phase of this (computed) effective pupil function in the transverse Fourier domain of the tomogram.

Previously, we utilized image metrics (analogous to sensor-less AO) to optimize the pupil correction that was expressed as a linear combination of Zernike polynomials.[11] A drawback of this approach is that when the number of Zernike polynomials is large (required for the correction of high-order aberrations), the resulting multi-dimensional global optimization becomes difficult to perform in real time. Additionally, the correction of the thick tissue aberrations has benefited from non-Zernike higher order corrections based on the more general segmented pupil

approach.[13] In this paper, we present a CAO method analogous to the use of natural guide stars in wavefront sensing AO for the correction of higher order monochromatic and chromatic aberrations, and demonstrate it in a sparse tissue phantom and in biological tissue.

Experimental data were acquired with a fiber-based spectral-domain OCT system based on a Michelson interferometer using a 50:50 coupler, but with astigmatic sample arm optics. The optical source was a 26 mW superluminescent diode (Praevium Research) with a center wavelength of 1330 nm and a bandwidth of 105 nm. The spectrometer (Bayspec, OCTS-1255-1330-1405) incorporated a 1024-pixel InGaAs linescan camera (Goodrich, LDH2), which was interfaced to the PC via a NI-IMAQ board (National Instruments, NI-PCIe 1427) and operated at an A-scan rate of 91 kHz and an exposure time of 6 μs. Identical doublet lenses with focal lengths of $f = 30$ mm (Thorlabs, AC254-030-C) were utilized in the sample arm for the collimating and objective lenses, resulting in a focal-plane resolution of $\sim 9\,\mu$m ($1/e^2$ spot size), Rayleigh range of 50 μm, and NA = 0.09 (at $1/e^2$ beam width). The beam was steered using an *x*-*y* galvanometer pair (SCANLAB, *SCAN*cube 7) interfaced to the PC via a multifunctional DAQ card (National Instruments, NI-PCIe 6353). A pair of cylindrical lenses with focal lengths of $f = 500$ mm (Thorlabs, LJ1144RM-C) and $f = -400$ mm (Thorlabs, LK1487RM-C) were inserted between the collimating lens and the galvanometer mirrors to provide astigmatism in the incident optical beam (astigmatism is a common aberration in retinal OCT). The axis and magnitude of the astigmatism was controllable via independent rotation of the cylindrical lenses about their optical axes. Three-dimensional data were acquired with an isotropic transverse sampling of 2 μm at a frame rate of 75 frames per second, corresponding to 1024 A-scans per B-mode image.

Reconstruction of aberration-corrected 3D tomograms consisted of the correction of astigmatism using a 3D filter based on Zernike polynomials[11] in the Fourier domain of the signal $S(Q_x, Q_y; k)$, followed by ISAM resampling to compute $S(Q_x, Q_y, Q_z)$,[9] and an inverse Fourier transform to the spatial domain. Correction of defocus with ISAM and low-order monochromatic aberrations with Zernike polynomials were beneficial (particularly in scattering tissues) to reveal any localized highly scattering point-like regions throughout the imaged volume that could serve as potential guide stars.

The amplitude and phase of a manually selected guide star were utilized to determine the effective and target (complex) PSFs, from which effective and target pupil functions were computed. The following procedure was applied in an iterative fashion to minimize the deviations between the effective and target pupils (see Fig. 1). Windowing was performed in the spatial domain to isolate the aberrated guide star signal $S_{GS}(x, y, z)$ and to compute a corresponding target PSF $S_T(x, y, z)$ as

$$S_{GS}(x, y, z) = w_{GS}(x, y, z)\, S(x, y, z), \tag{1}$$

$$S_T(x, y, z) = w_T(x, y, z)\, S(x, y, z), \tag{2}$$

where w_{GS} and w_T are Gaussian windows with full-width-half-maxima of $(10 \times 10 \times 16)$ μm and $(1 \times 1 \times 1.4)$ μm along the $(x \times y \times z)$ dimensions, respectively. The target PSF thus had the same amplitude and phase as the peak of the guide star, but the reduced (sub-resolution) width allowed the ideal local "impulse response" to be evaluated (from the Fourier shift theorem this impulse response results in a linear phase ramp in the Fourier domain with slope determined by the 3D spatial position of the guide star). Working in the Fourier domain of the data provided independent access to the amplitude or phase of the effective 3D pupil. Consequently, three-dimensional Fourier transforms of S_{GS} and S_T were performed to compute the effective and the target 3D pupils. An aberration correction filter $H_{AC}(Q_x, Q_y, Q_z)$ was calculated via phase conjugation of the deviation of the effective pupil from the target pupil as

$$\Phi(Q_x, Q_y, Q_z) = \arg\{\tilde{\tilde{S}}_{GS}(Q_x, Q_y, Q_z)\tilde{\tilde{S}}^*_T(Q_x, Q_y, Q_z)\}, \tag{3}$$

$$H_{AC}(Q_x, Q_y, Q_z) = \exp\{-i\,\Phi(Q_x, Q_y, Q_z)\}, \tag{4}$$

where the double tilde ($\tilde{\tilde{}}$) denotes a 3D Fourier transform and the asterisk (*) denotes the complex conjugate. Aberrations of the effective pupil function were deconvolved by multiplying the Fourier domain signal $S(Q_x, Q_y, Q_z)$ with $H_{AC}(Q_x, Q_y, Q_z)$.

Figure 2 shows results of CAO in a silicone phantom consisting of 1 μm titanium dioxide scatterers. The *en face* image with standard OCT processing clearly shows a line structure associated with astigmatism. After the astigmatism correction, these aberrated line-shaped PSFs are transformed into circularly symmetric PSFs, albeit with defocus still present. The subsequent application of ISAM corrects defocus throughout the acquired volume. However, the PSFs in Fig. 2(c) show evidence of side lobe structures associated with higher order aberrations. These aberrations are likely due to the optical system which utilized cost-effective achromatic doublets rather than well-corrected microscope

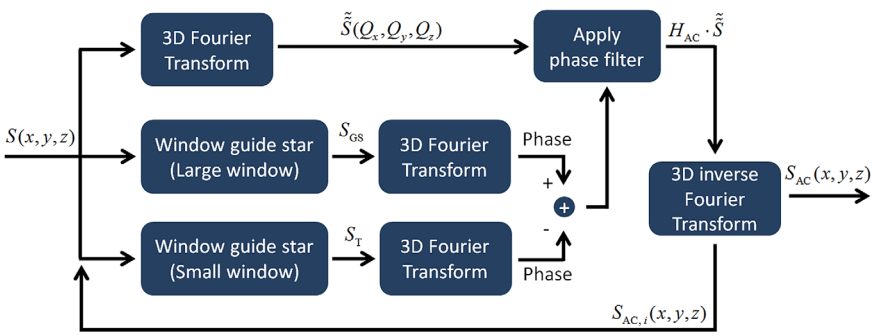

FIG. 1. Flow chart of iterative guide-star-based CAO. The aberration-corrected signal after the i^{th} iteration is denoted $S_{AC,i}(x, y, z)$, and the final output is denoted as $S_{AC}(x, y, z)$. Arguments of the variables $S_{GS}(x, y, z)$, $S_T(x, y, z)$, $H_{AC}(Q_x, Q_y, Q_z)$, and $\tilde{\tilde{S}}(Q_x, Q_y, Q_z)$ have been suppressed.

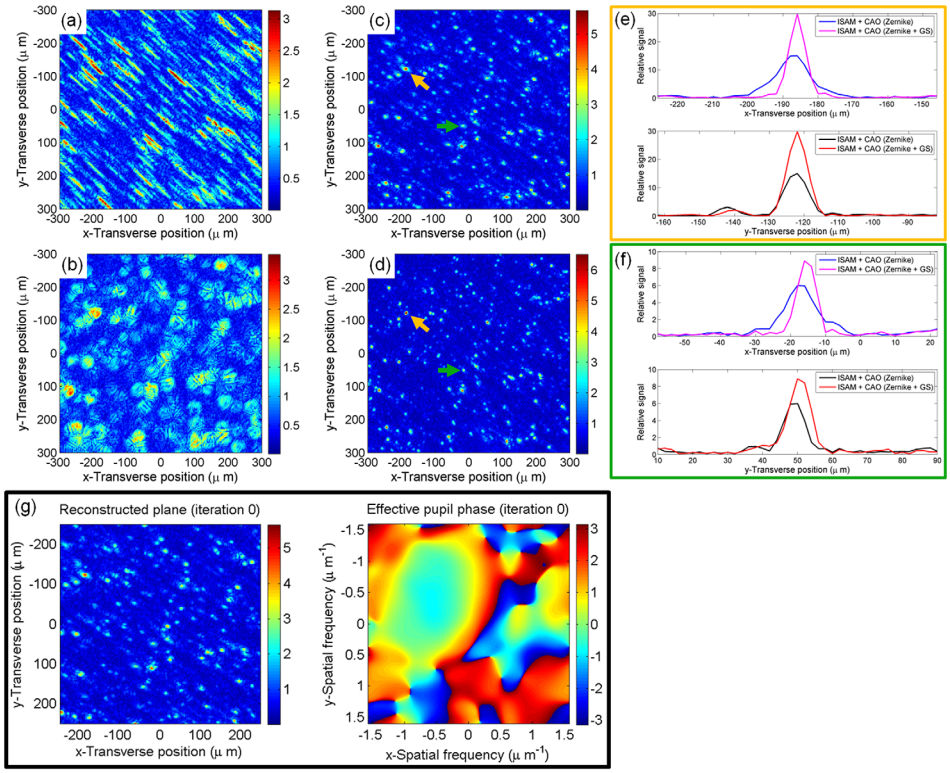

FIG. 2. Guide-star-based CAO in a silicone phantom consisting of sub-resolution microparticles, using a 3D dataset that was acquired with an astigmatic optical system. *En face* planes 574 μm (optical depth, surface of the sample at 975 μm) above the plane of least confusion. (a) OCT, (b) OCT with Zernike-based astigmatism correction, (c) ISAM with Zernike-based astigmatism correction, and (d) GS-CAO of higher order aberrations using the 3D ISAM dataset incorporating Zernike-based correction. Horizontal and vertical cross-sections (e) through the guide star used for aberration correction (orange arrows in (c) and (d)), and (f) through a different scatterer in the field-of-view (green arrows in (c) and (d)). (g) Zoomed *en face* ISAM image and effective pupil function for the central value of Q_z, and animation of GS-CAO over 5 iterations. Gamma correction ($\gamma = 0.6$) was applied to the intensity scale of the *en face* images to compress dynamic range, whereas the vertical axis of the cross-sectional plots are shown on a linear scale (enhanced online) [URL: http://dx.doi.org/10.1063/1.4768778.1].

objectives. Figures 2(d)–2(f) show that after 5 iterations of Guide-star-based computational adaptive optics (GS-CAO) (guide star indicated by orange arrow), there is clearly a narrowing of the PSF and increased signal-to-noise ratio (SNR). This improvement was seen over a relatively wide field-of-view (>500 μm), and range of depths (770 μm, data not shown), indicating that in this low-scattering sparse sample, a single aberration correction filter (multiplication of the filters from each iteration) is valid over a relatively large *isotome*[14] (discussed in a separate paragraph below).

Figure 2(g) shows an animation of iterative GS-CAO. It can be seen that the PSF narrowing and SNR increase with increasing iteration number is associated with a flattening of the effective pupil phase, indicating the restoration of constructive interference across the spatial frequency bandwidth.

Figure 3 demonstrates CAO in highly scattering rabbit muscle tissue, showing the *en face* plane containing a bright scatterer that was selected as the guide star. (Similar naturally occurring point-like structures, albeit with lower scattering amplitude, were present throughout the ISAM-reconstructed volume.) As with the phantom, we see (from Figs. 3(a) and 3(b)) that the correction of astigmatism transforms linear streak-like PSFs into circularly symmetric

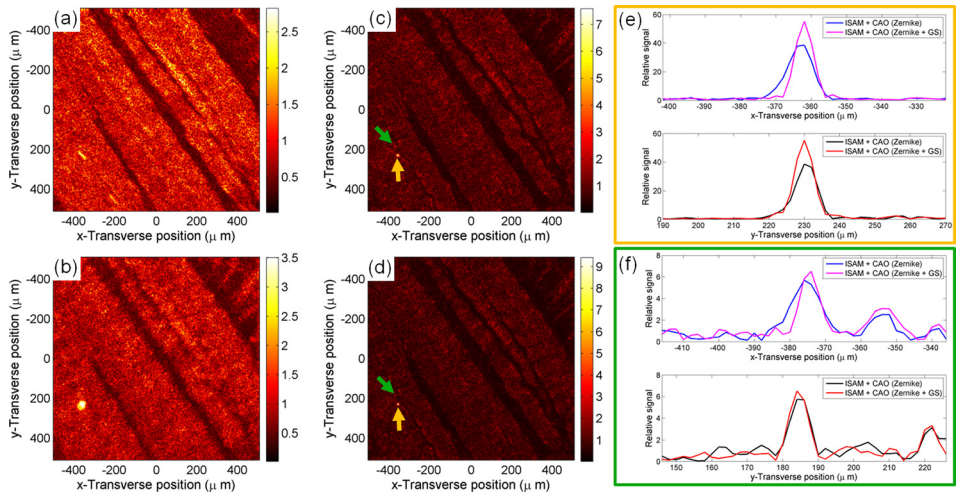

FIG. 3. Guide-star-based CAO of a 3D rabbit muscle tissue dataset acquired with an astigmatic optical system. *En face* planes 574 μm (optical depth, surface of the sample at 600 μm) above the plane of least confusion are shown after (a) OCT, (b) OCT after Zernike-based astigmatism correction, (c) ISAM after Zernike-based astigmatism correction and (d) GS-CAO correction of higher order aberrations using the 3D ISAM dataset incorporating the Zernike-based correction. Horizontal and vertical cross-sections (e) through the guide star used for aberration correction (orange arrows in (c) and (d)), and (f) through a different scatterer in the field-of-view (green arrows in (c) and (d)). Gamma correction ($\gamma = 0.6$) was applied to the intensity scale of the *en face* images to compress dynamic range, whereas the vertical axis of the cross-sectional plots are shown on a linear scale.

PSFs, and that ISAM (see Fig. 3(c)) produces fine tissue structure previously not visible. The application of GS-CAO clearly increases the signal of the guide star and therefore produces an image with increased dynamic range (responsible for the apparent "dimming" of the image in Fig. 3(d)). Quantitative plots in Figs. 3(e) and 3(f) show the improvement in resolution and SNR at the guide star location. The nearby location also shows improved resolution and SNR, but the improvement is not as significant as in the phantom results. In this case, this is because the windowing operation does not isolate signal from an ideal point scatterer within the muscle tissue, but includes signal from surrounding regions as well.

We investigated the ability of GS-CAO to resolve fine tissue structure, both in the same plane as the guide star and at other planes within the 3D dataset. Figure 4 compares the starting ISAM images and guide star corrected images, and highlights fine tissue structure that is more clearly resolved after GS-CAO. In some instances fine tissue structure, such as the delineation of different muscle fiber bundles in Figs. 4(b), 4(d), 4(f)), can now be seen. The alignment of this structure with the known axis of the muscle fiber bundles strongly suggests that they are not artifacts.

The aberration correction filter in Eq. (4), based on the concept of a generalized 3D pupil,[15] encodes information about monochromatic as well as chromatic aberration. Mitigation of chromatic aberration is of importance for broadband imaging systems since it manifests both as longitudinal blur (along the z-axis), as well as blurring in the transverse plane. Previously, CAO treated the k-dependence of the 3D aberration correction filter as a simple scaling of the monochromatic transverse phase function described by a linear combination of Zernike polynomials. With GS-CAO, the aberration filter can support arbitrary 3D phase functions. It should be noted that this correction of chromatic aberration is similar to numerical dispersion correction in OCT.[16] However, this chromatic aberration correction goes beyond dispersion correction in OCT, since it has a dependence on the transverse coordinates (Q_x, Q_y) of the effective 3D pupil. In contrast, dispersion correction is a one-dimensional correction along the k-axis of the spectral data $S(x, y; k)$, and can be thought of as a subset of this chromatic aberration correction.

For this work, we utilized phase-only deconvolution due to the practical considerations mentioned below, and to clearly demonstrate that the signal increase in the spatial domain is due to the restoration of constructive interference across the Fourier bandwidth, rather than a modification of the Fourier amplitudes. In principle, the effective pupil function can manifest amplitude structure due to aberrations, even if the pupil function is a phase-only function. Correction of this amplitude structure requires regularization of the deconvolution operation. Further work is required to investigate the role of amplitude and phase deconvolution and (potentially sample dependent and spatially varying) regularization on the reconstruction accuracy and quality.

The term *isotome*[14] (or *isotomic volume*) used here in the context of volumetric tomography is a generalization of the term *isoplanatic patch*[1] utilized in astronomical AO to describe the angular extent over which atmospheric wavefront disturbances can be considered identical. An imaging system may be considered *isoplanatic* if the condition of space-invariance holds,[12] i.e., a single filtering operation can be performed to produce optimal resolution throughout the transverse field-of-view. By extension, an isotome can be considered as the range of 3D space over which a single aberration-correction filter can be used to provide diffraction-limited resolution. The isotomic volume can be limited by spatially varying aberrations, such as sample-induced aberrations, or sample dispersion. Indeed, spatially varying sample dispersion can also result in a non-unique OCT or ISAM reconstruction.

In principle, it is possible to perform GS-CAO in a single step, i.e., without iteration. If the separation of scatterers is large compared to the aberrated PSF width, then it is possible to isolate most of the aberrated signal associated with a given scatterer in a single windowing operation. In practice, in order to isolate the signal of a given scatterer from neighboring regions, it is desirable to use a window that is smaller than the full aberrated extent of the PSF. The overlap of neighboring PSFs corrupt the calculation of the effective pupil function since this computed pupil is then based on an extended rather than a point source. As the number of iterations increases, a greater fraction of the PSF "energy" will fall within the window S_{GS}, resulting in improved aberration correction.

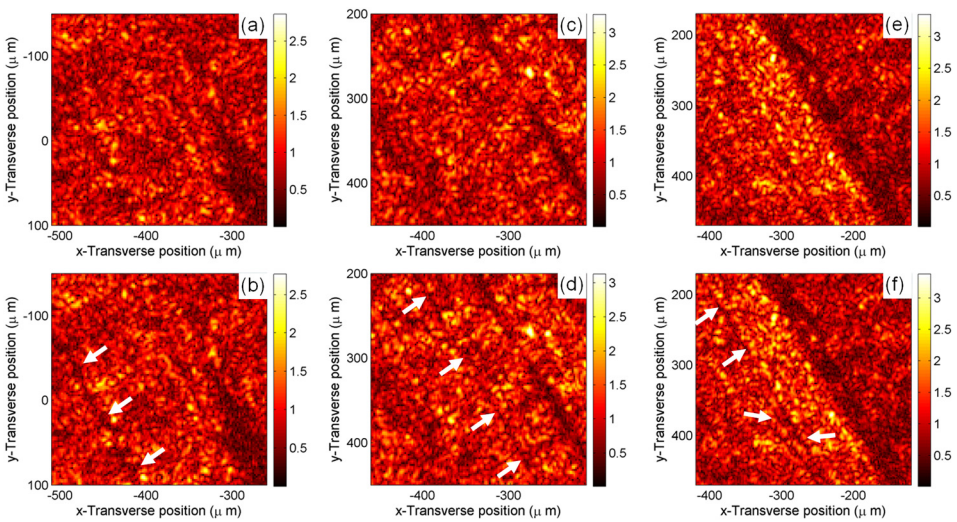

FIG. 4. Zoomed regions of *en face* planes extracted from the 3D reconstructions of the rabbit muscle dataset shown in Fig. 3. (Top row) ISAM with Zernike-based astigmatism correction, and (bottom row) with additional GS-CAO using the same guide star from Fig. 3. The images above were extracted from (optical) depths of (a and b) 574 μm, (c and d) 513 μm, and (e and f) 475 μm above the plane of least confusion. The white arrows in (b, d, and f) denote tissue structure that is more clearly resolved after GS-CAO. Gamma correction ($\gamma = 0.6$) was applied to the intensity scale of the images in order to compress dynamic range.

Real-time implementation of GS-CAO is achievable through the processing of smaller volumes. Equations (1)–(4) do not require the use of a complete 3D tomogram. The results presented in this paper were generated from ISAM-processed 3D datasets spanning the full transverse range but only 2.5 mm in depth. These were extracted from the full 2.8 mm depth range supported by the spectral resolution of our spectrometer. Alternatively, by omitting chromatic aberration correction, monochromatic aberrations can be corrected for individual *en face* planes (i.e., on $S(x, y, z_i)$at depth z_i), using 2D effective and target pupil functions.

The Fourier transform relationship between the pupil function and the optical field at focus not only forms the basis of CAO, but also provides insight into hardware-based AO and related techniques for focusing in scattering (turbid) media. In CAO, aberrations of the effective pupil function calculated from the effective PSF are corrected through deconvolution. The physical operation of wavefront shaping in hardware-based AO can thus be thought of as a deconvolution of aberrations associated with the optical beam. Indeed this deconvolution, written as a phase conjugation of aberrations in Eq. (4), also forms the basis of phase conjugation methods for focusing in turbid media.[17] Additionally, these phase conjugation methods have been shown to be equivalent to time reversal, as implemented for iterative acoustic focusing on different targets in a multi-target medium[18] and time-reversal imaging based on acoustic speckle.[19]

Traditionally, optical imaging and microscopy has relied heavily on the manipulation of optical wavefronts using hardware such as lenses and mirrors to optimize image quality. This work provides further evidence for the importance of computational techniques for the post-acquisition (virtual) manipulation of optical wavefronts (i.e., based on the recording of complex optical fields and the physics of wave propagation). Guide-star-based CAO using a 3D effective pupil allows the correction of both monochromatic and chromatic aberrations. Results in a sparse phantom showed significant improvement in resolution and SNR over a large isotome, while highly scattering muscle tissue showed improved resolution of fine structure over an extended volume. This method could be utilized in the future for quantifying the dimensions of isotomic volumes in tissue, since these are expected to be reduced with increasing depth and turbidity. Future work will also explore the synergies between hardware and computational approaches, e.g., by prioritizing optical system design that optimizes signal over an extended volume rather than minimizing aberrations. The conceptual framework shared with phase conjugation and time-reversal methods suggests that it is also worth investigating the use of CAO for turbidity suppression and time-reversal tomographic imaging deep in scattering tissue.

The authors thank Eric Chaney and Dr. Marina Marjanovic for providing the muscle tissue used in this study, which was acquired under a protocol approved by the Institutional Animal Care and Use Committee at the University of Illinois at Urbana-Champaign. We also thank Dr. Daniel Marks for providing the phantom used in this study and Darold Spillman for providing operations and information technology support. B.W.G. was supported by the Predoctoral National Institutes of Health Environmental Health Sciences Training Program in Endocrine, Developmental, and Reproductive Toxicology at the University of Illinois at Urbana-Champaign. This research was supported in part by grants from the National Institutes of Health (R01 EB012479 and R01 EB013723). Additional information can be found at http://biophotonics.illinois.edu.

[1]J. M. Beckers, Annu. Rev. Astron. Astrophys. **31**, 13 (1993).
[2]C. E. Max, S. S. Olivier, H. W. Friedman, K. An, K. Avicola, B. V. Beeman, H. D. Bissinger, J. M. Brase, G. V. Erbert, D. T. Gavel, K. Kanz, M. C. Liu, B. Macintosh, K. P. Neeb, J. Patience, and K. E. Waltjen, Science **277**(5332), 1649 (1997).
[3]M. Rueckel, J. A. Mack-Bucher, and W. Denk, Proc. Natl. Acad. Sci. USA **103**(46), 17137 (2006); M. J. Booth, M. A. A. Neil, R. Juskaitis, and T. Wilson, Proc. Natl. Acad. of Sci. USA **99**(9), 5788 (2002); P. Kner, J. W. Sedat, D. A. Agard, and Z. Kam, J. Microsc. **237**(2), 136 (2010); A. J. Wright, S. P. Poland, J. M. Girkin, C. W. Freudiger, C. L. Evans, and X. S. Xie, Opt. Express **15**(26), 18209 (2007); A. Roorda, F. Romero-Borja, W. J. Donnelly, H. Queener, T. J. Hebert, and M. C. W. Campbell, Opt. Express **10**(9), 405 (2002).
[4]B. Hermann, E. J. Fernandez, A. Unterhuber, H. Sattmann, A. F. Fercher, W. Drexler, P. M. Prieto, and P. Artal, Opt. Lett. **29**(18), 2142 (2004); Y. Zhang, B. Cense, J. Rha, R. S. Jonnal, W. Gao, R. J. Zawadzki, J. S. Werner, S. Jones, S. Olivier, and D. T. Miller, Opt. Express **14**(10), 4380 (2006).
[5]Y. Zhang, J. T. Rha, R. S. Jonnal, and D. T. Miller, Opt. Express **13**(12), 4792 (2005); E. J. Fernandez, B. Hermann, B. Povazay, A. Unterhuber, H. Sattmann, B. Hofer, P. K. Ahnelt, and W. Drexler, Opt. Express **16**(15), 11083 (2008).
[6]M. J. Booth, Opt. Express **14**(4), 1339 (2006); D. Debarre, M. J. Booth, and T. Wilson, Opt. Express **15**(13), 8176 (2007); D. Debarre, E. J. Botcherby, T. Watanabe, S. Srinivas, M. J. Booth, and T. Wilson, Opt. Lett. **34**(16), 2495 (2009).
[7]T. Colomb, F. Montfort, J. Kuhn, N. Aspert, E. Cuche, A. Marian, F. Charriere, S. Bourquin, P. Marquet, and C. Depeursinge, J. Opt. Soc. Am. A **23**(12), 3177 (2006); L. Miccio, D. Alfieri, S. Grilli, P. Ferraro, A. Finizio, L. De Petrocellis, and S. D. Nicola, Appl. Phys. Lett. **90**(4), 041104 (2007); U. Schnars and W. P. O. Juptner, Meas. Sci. Technol. **13**(9), R85 (2002).
[8]L. F. Yu, B. Rao, J. Zhang, J. P. Su, Q. Wang, S. G. Guo, and Z. P. Chen, Opt. Express **15**(12), 7634 (2007); Y. Yasuno, J. I. Sugisaka, Y. Sando, Y. Nakamura, S. Makita, M. Itoh, and T. Yatagai, Opt. Express **14**(3), 1006 (2006); D. Hillmann, C. Luhrs, T. Bonin, P. Koch, and G. Huttmann, Opt. Lett. **36**(13), 2390 (2011).
[9]T. S. Ralston, D. L. Marks, P. S. Carney, and S. A. Boppart, Nature Phys. **3**(2), 129 (2007).
[10]T. S. Ralston, S. G. Adie, D. L. Marks, S. A. Boppart, and P. S. Carney, Opt. Lett. **35**(10), 1683 (2010); T. S. Ralston, D. L. Marks, P. S. Carney, and S. A. Boppart, Opt. Express **16**(4), 2555 (2008); B. J. Davis, S. C. Schlachter, D. L. Marks, T. S. Ralston, S. A. Boppart, and P. S. Carney, J. Opt. Soc. Am. A **24**(9), 2527 (2007).
[11]S. G. Adie, B. W. Graf, A. Ahmad, P. S. Carney, and S. A. Boppart, Proc. Natl. Acad. Sci. USA **109**(19), 7175 (2012).
[12]J. W. Goodman, *Introduction to Fourier Optics*, 2nd ed. (McGraw-Hill San Francisco, 1996), pp. 21, 135–137, 145–146.
[13]N. Ji, D. E. Milkie, and E. Betzig, Nature Methods **7**(2), 141 (2010).
[14]B. R. Frieden, J. Opt. Soc. Am. **57**(1), 56 (1967).
[15]C. W. McCutchen, J. Opt. Soc. Am. **54**(2), 240 (1964); Z. Kam, B. Hanser, M. G. L. Gustafsson, D. A. Agard, and J. W. Sedat, Proc. Natl. Acad. Sci. USA **98**(7), 3790 (2001).
[16]A. F. Fercher, C. K. Hitzenberger, M. Sticker, R. Zawadzki, B. Karamata, and T. Lasser, Opt. Express **9**(12), 610 (2001); D. L. Marks, A. L. Oldenburg, J. J. Reynolds, and S. A. Boppart, Appl. Opt. **42**(2), 204 (2003).
[17]Z. Yaqoob, D. Psaltis, M. S. Feld, and C. H. Yang, Nature Photonics **2**(2), 110 (2008); I. M. Vellekoop, A. Lagendijk, and A. P. Mosk, Nat. Photonics **4**(5), 320 (2010).
[18]M. Fink, D. Cassereau, A. Derode, C. Prada, P. Roux, M. Tanter, J. L. Thomas, and F. Wu, Rep. Prog. Phys. **63**(12), 1933 (2000).
[19]G. Montaldo, M. Tanter, and M. Fink, Phys. Rev. Lett. **106**(5), 054301 (2011).